Rupture of intermetallic networks and strain localization in cast AlSi12Ni alloy: 2D and 3D characterization

Aly Tireira, G. Requena, S. Sao Joao, Andras Borbely, Helmut Klöcker

Rupture of intermetallic networks and strain localization in cast AlSi12Ni alloy: 2D and 3D characterization

A. Tireira [a], G. Requena [b], S. Sao Jao [a], A. Borbely [a], H. Klocker [a, *]

[a] *Ecole des Mines de Saint-Etienne, 158 Cours Fauriel, St-Etienne 42023, France*
[b] *German Aerospace Centre, Institute of Materials Research, Linder Höhe, 51147 Cologne, Germany*

Damage development during tensile straining of a cast AlSi12Ni alloy has been characterized by in situ SEM imaging and synchrotron X-ray microtomography. Two main damage mechanisms consisting of intermetallic particle rupture and decohesion of Al-Si interfaces were revealed. Particle rupture takes place already from the beginning of the deformation, while decohesion of Al-Si interfaces is more characteristic at later stages. It is shown that damage evolution in the alloy is closely related to the underlying geometry of the intermetallic phase, its clustered structure playing a double role in con-trolling strain localization in the matrix as well as the rupture sequence of the intermetallic phase itself. The latter shows that small clusters break-off from the complex intermetallic network before large clusters, in good agreement with their load carrying capacity determined by the local volume fraction of the intermetallic phase. Finite element modeling of the alloy's tensile behavior evidences that defor-mation bands formed in the alloy with complex structure are similar to those developed in a model particle reinforced metal-matrix composite, where the particles correspond to the clustered regions of the intermetallic phase.

1. Introduction

Cast Al-Si alloys are widely used in the automotive industry for cylinder heads, pistons and engine crankcases due to their excellent castability as well as lower weight and better heat transfer compared to cast iron. The silicon content in standardized commercial cast alloys is in the range of 7–23 wt%, which leads to a range of typical hypoeutectic, eutectic and hypereutectic structures [1]. Their microstructure is made up of an α-Al matrix containing several rigid phases. For example, the eutectic and primary Si solidify as almost pure phases of this element and can have different morphologies: compact massive particles in hypereutectic alloys and branched plates in those with near-eutectic Si concentrations [2–4]. Furthermore, three dimensional (3D) interconnected networks of brittle intermetallic (IM) phases can form depending on the chemical composition of the alloy (e.g. Al_9FeNi and $Al_{15}Si_2(FeMn)_3$) [5]. These networks are usually connected to the eutectic and the primary Si leading to a rigid and highly interpenetrating structure. Due to their brittleness the 3D networks can easily break during thermo-mechanical loading, which leads to damage accumulation and crack formation [2–4]. In this context predictive models accounting for the complex real microstructure and capable to describe initiation as well as evolution of damage are stringently needed. It is well known that strain localization and damage are strongly interrelated, however, it is less known how are they influenced by the geometrical characteristics of the underlying structure (for instance by the geometry of the hard phase, which in the present case is represented by the network of rigid phases). It is the aim of the present work to explore this connection through two distinct characterization techniques. First, 2D Digital Image Correlation (DIC) analysis is applied to Scanning Electron Microscopy (SEM) images taken during in situ tensile deformation of the specimen. Since SEM images characterize the surface of the samples their analysis allows obtaining only qualitative information on damage. To perform a quantitative analysis 3D micro-tomography scans were made during in situ tensile straining of the same material at synchrotron source. Damage analysis of these 3D volumes was done with two original algorithms. The first one characterized the break-up of the rigid IM phases by tracking a parent particle and its subsequently broken parts (sons) during deformation, while the second carried out a geometrical analysis of the complex IM

* Corresponding author.
E-mail address: klocker@emse.fr (H. Klocker).

structure determining its clustered regions. Finally, Finite Element Modeling (FEM) of the plastic behavior of the alloy with highly complex structure allows gaining insight into the role played by the hard IM phases on strain localization.

2. Experimental

2.1. Material and microstructure

An AlSi12Ni alloy with chemical composition as given in Table 1 was produced by squeeze casting. The material was investigated at room temperature after Spheroidization heat Treatment (ST) at 540 °C during 24 h followed by air cooling. After ST the alloy was subjected to artificial aging at 300 °C for 2 h followed by furnace cooling to stabilize the precipitates. The microstructure of the alloy consists of an α-Al matrix and of about 20 vol% of rigid phases: ~8 vol% of primary Al_9FeNi and $Al_{15}Si_2(FeMn)_3$ IM phases and ~12 vol% of eutectic Si [6]. Both type of IMs present similar values of hardness of about 8 and 11 GPa, respectively [7] close to that of Si of 11 GPa. As evidenced by Asghar et al. [6] ST affects mainly the Si phase, which coarsens and becomes more globular, while the geometry of the IM phases is only slightly affected. The global evolution of the microstructure, however, leads to increased ductility in the detriment of strength.

The 3D structure of the different phases was first characterized by X-ray micro-tomography at the ID19 beamline of the European Synchrotron Radiation Facility (ESRF). The details of acquisition conditions were described in Ref. [5]. The reconstructed volume had a size of 2048^3 voxels (614^3 μm^3), with a voxel size of $(0.3\ \mu m)^3$. The phase contrast available at this beamline made possible the separate segmentation of the eutectic Si and the Al matrix, which have nearly equal X-ray absorption coefficients. The IM phases could be easily detected due to their higher absorption. The reconstructed volumes were analyzed with ImageJ [8] and self-developed Matlab functions, such as median filtering and adaptive segmentation [9,10]. The IM and the Si phases were extracted as binary images and are shown in Fig. 1a and b, respectively (the images were created with AMIRA [11]). They constitute a complex and highly interpenetrating 3D network (Fig. 1c).

2.2. 2D in situ observation of damage and strain localization

Particle break-up and strain localization during tensile loading were first characterized by 2D in situ observations in the SEM. The analyzed specimens had a gauge length of 5 mm and a rectangular cross section of 0.68×3 mm^2. The Region of Interest (ROI) followed by SEM imaging was located at the middle of the gauge length and extended over an area of about 3×3 mm^2. The sample was also foreseen with a cylindrical notch of radius equal to 0.2 mm, which induced a stress concentration factor of about 3 and permitted capturing damage evolution at the middle of the gauge length. Fig. 2 shows the in situ stress-strain curve, where the bursts indicate load relaxation taking place during image acquisition. Typical damage mechanisms observed during the test are shown in Fig. 3. Already at small overall strains of 2% the IM phase breaks (Fig. 3a and b) and decohesion events of the Si-Al matrix interface are taking place. At larger strains (of about 8%) deformation localizes between IM clusters (or packets) leading to significant local shear (Fig. 3c). It is important to note that in such regions the Si phase moves together with the Al matrix and Si particles align parallel to the maximum shear direction.

Table 1
Chemical composition of the studied AlSi12Ni alloy (in wt.%).

Si	Ni	Fe	Mn	Al
11.92	1.22	0.69	0.27	Bal.

Strain localization was quantified by DIC [12–15] based on a rectangular mesh with an element size of 20 μm × 20 μm (marked by a yellow square in Fig. 4a), which was large enough to contain several patterns, but also sufficiently small permitting to capture strain gradients. Before determining the displacement field by DIC a Gaussian averaging filter was applied to each image to reduce acquisition noise. Typical strain maps (Fig. 4a) clearly emphasize the significant screening caused by the IM phases. Regions with high IM phase content are quasi non-deformable, while IM-free regions are subject to high strains experiencing significant shear deformation (Fig. 4b). As emphasized above shear bands form in matrix regions containing Si and Al. Fig. 5 highlights the difference between local strains at two selected points P_1 and P_2 located inside these particular regions. Compared to the applied strain ($\varepsilon_{applied}$) the local equivalent strain (ε_{loc}) at P_1 is larger by a factor of about 1.5, while strain at P_2 remains smaller by a factor of about 3.

DIC analysis of SEM images allows a pertinent, but only qualitative description of damage. One can conclude for example on the existence of two damage mechanisms, i.e. rupture of IM phases and decohesion of Si-Al interfaces. Both mechanisms are already active shortly after the begin of plastic yielding, but their relative contribution to the total damage changes as a function of applied strain. IM phase break-up is dominant at smaller strains, while interface decohesion is more characteristic towards the end of the test when it leads to crack formation. It was also recognized that strain localization is controlled by the spatial distribution of the IM phase. In order to better understand this phenomenon in situ characterization of IM phase damage was done at synchrotron source using on 3D micro-tomography.

2.3. 3D in situ characterization of particle break-up during tensile loading

A tensile test coupled with microtomography was performed in situ at the ID15 beamline of the ESRF on a sample with a cross section of 1×1 mm^2 and a gauge length of 30 mm (Fig. 6). Tomography scans were performed using a pink X-ray beam provided by an undulator source. 850 equidistant projections were taken during 180° rotation of the sample using an exposure time of 18 m per projection resulting in a total scanning time of about 20 s per volume. The total reconstructed volume was of about $1.4 \times 1.4 \times 1.1$ mm^3 ($1027 \times 1027 \times 801$ voxels with a voxel size of $(1.4\ \mu m)^3$). Due to the limited field of view of the detector (1.4×1.1 mm^2) an ellipsoidal notch with 0.08 mm minor axis and 0.15 mm major axis was created at the center of one lateral surface of the sample and the detector was centered on the notch. The stress concentration factor around the notch permitted to visualize damage progression in the selected volume from the first events of IM break-up until crack formation. 28 scans were acquired during the tensile test performed with a dedicated load frame [16]. The locations of the analyzed states are indicated by square symbols on the stress-strain curve shown in Fig. 6. Compared to the stress-strain curve of the sample deformed in the SEM (Fig. 2) both the tensile strength and the ductility are lower, which is a consequence of the higher stress concentration factor at the notch (4.75 and 3 for tests at ESRF and in the SEM, respectively).

Fig. 7a shows the tomographic reconstruction corresponding to state no. 1 (before deformation). The IM particles appear in light gray, while the Al matrix and the Si phase in dark gray. Although some edge enhancement effect is present in these scans, the silicon phase is only slightly darker than the matrix and could not be segmented independently. The IM phases, however, due to their

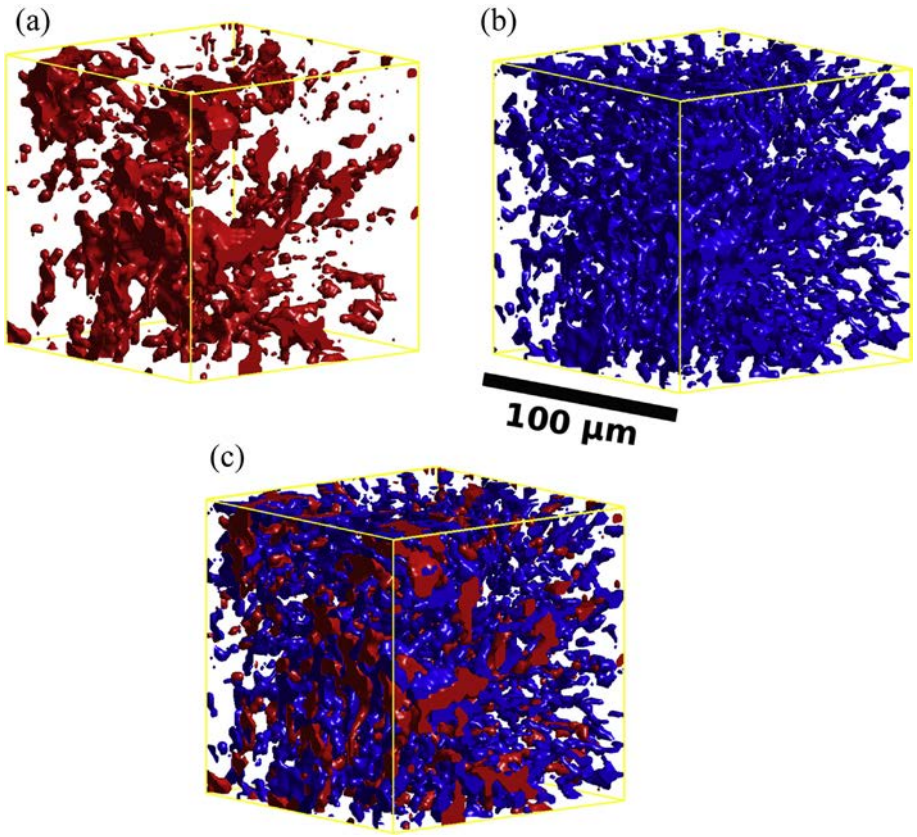

Fig. 1. 3D structure of the reinforcing phases present in the AlSi12Ni alloy after ST. (a) The IM network, (b) eutectic Si (c) interpenetrating network of IM and Si phases.

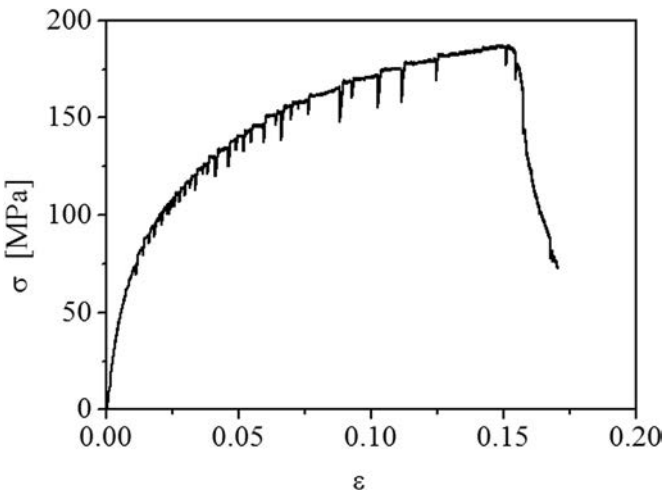

Fig. 2. Stress-strain curve of the specimen deformed in situ in the SEM.

higher absorption coefficient could be well segmented using the local threshold algorithm [5] applied previously to ex situ samples. On different cuts through the volume the IM phase shows up as "particles" (Fig. 7b), but in reality it forms a complex, interconnected architecture composed of thin branches spread through the entire reconstructed volume (Fig. 1). The analysis of this complex 3D structure and its role played in strain localization and damage sequence represents therefore a real challenge. To answer these questions two new algorithms were developed.

3. Algorithms for characterizing IM phase break-up and its clustered structure

3.1. Particle tracking algorithm

Visual analysis of SEM images suggests that break-up of IM "particles" is the dominant damage mechanism at small strains. Its proper quantitative characterization, however, can only be performed on the 3D structure capturing the real "particle" shape and volume. Additionally, describing damage evolution requires the genealogy of broken elements, i.e. the progression of all broken parts (sons) of an initially intact "particle" through all reconstructed states. To perform this analysis first a ROI in the state i, was chosen and the IM particles were labeled (Fig. 8a). The position of the ROI in the volume corresponding to state i+1 was determined by cross correlation. The ROI was displaced through a larger volume Ω of the later state (Fig. 8b) and the displacement leading to the maximum value of the correlation coefficient was retained:

$$C(\boldsymbol{u}) = \frac{\sum_x \sum_u (f(x) - f_m)(g(x+u) - g_m)}{\sqrt{\sum_x (f(\boldsymbol{x}) - f_m)^2} \sqrt{\sum_x (g(x) - g_m)^2}} \quad (1)$$

where f and g are the gray values in the images corresponding to states i and $(i+1)$, while f_m and g_m are their mean values over the considered ROI. The normalization by the corresponding standard deviations eliminates the influence of intensity variation. The next step was the determination of the genealogy of each particle. Based on the displacement $\boldsymbol{u}$ corresponding to the maximum correlation coefficient the ROI of state $(i+1)$ was placed in the volume of state i and the intersections between IM particles were determined. Usually, a given particle in state i can intersect several particles at

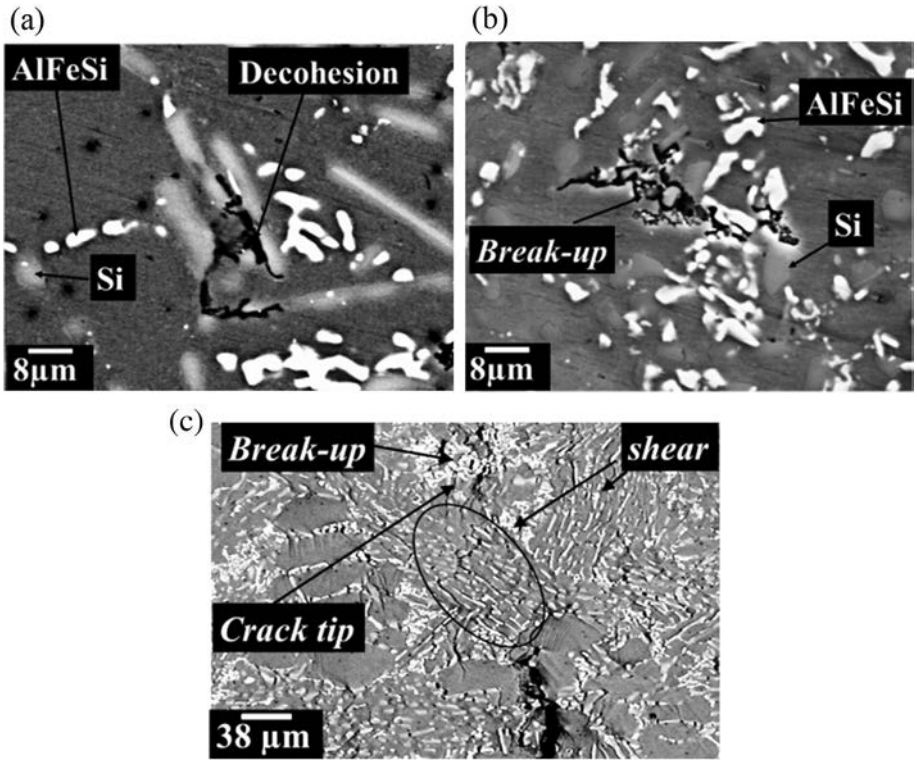

Fig. 3. Damage mechanisms identified on SEM images. a) Decohesion of Si and α-Al matrix interface and b) IM phase break-up at an applied strain of 2%. c) Strain localization and crack formation at an applied strain of 8% (the applied load points in the horizontal direction on the figures).

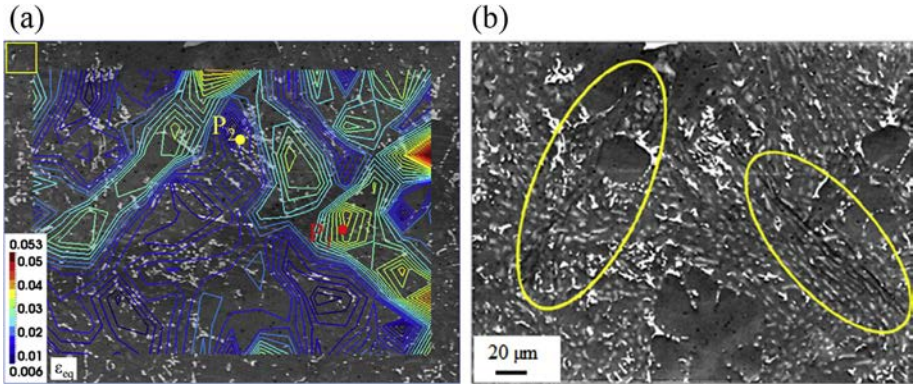

Fig. 4. (a) Equivalent strain distribution obtained by 2D-DIC superposed on the undeformed microstructure (the yellow square at the top-left corner indicates the size of the mesh used for DIC). (b) Strain localization bands formed in the IM-free region. The images correspond to an applied strain of 0.018. (For interpretation of the references to color in this figure legend, the reader is referred to the web version of this article.)

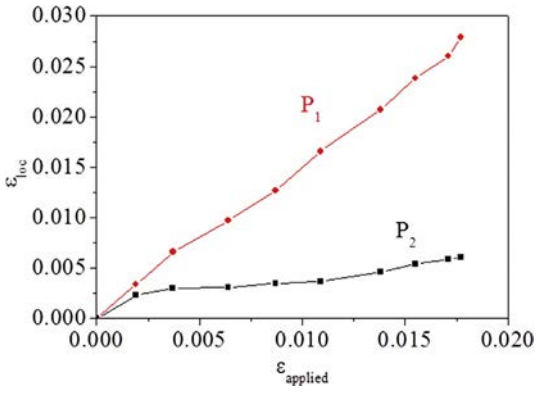

Fig. 5. Equivalent strain at two particular points as a function of the applied strain. P_1 is located at an "IM-free zone" while P_2 inside of an IM cluster (Fig. 4a).

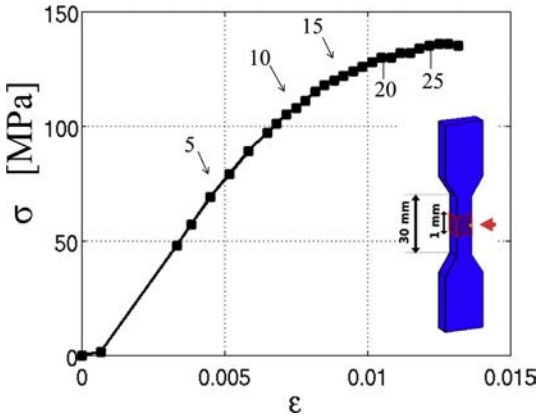

Fig. 6. Stress-strain curve and geometry of the specimen deformed at ESRF. The arrow indicates the position of the notch.

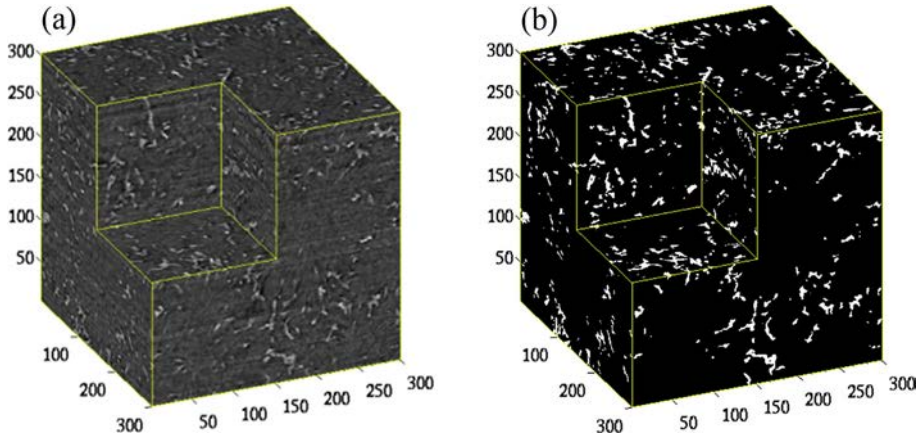

Fig. 7. (a) Tomographic reconstruction of state 1, and (b) segmented "IM particles", which in reality form a complex interconnected 3D structure. The dimensions of the reconstruction are given in units of voxels (1 voxel = 1.4^3 μm^3).

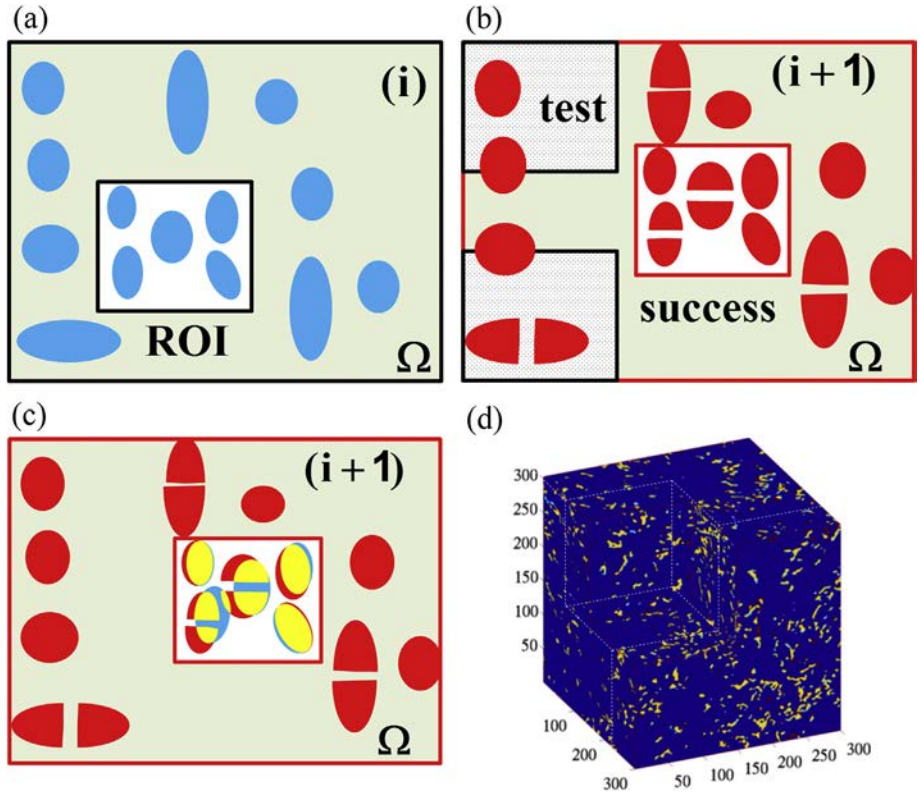

Fig. 8. Tracking algorithm. (a) Choice of the ROI at state *i*. (b) Cross-correlation with the volume at state $(i + 1)$. (c) Determination of IM intersections. Parent and son particles are in light blue and red, respectively. Intersections between parents and sons are in yellow. (d) Superposition of IM particles of states 7 and 8 showing the parents (light blue), sons (red) and their intersections (in yellow). (units are given in voxels, 1 voxel = 1.4^3 μm^3). (For interpretation of the references to color in this figure legend, the reader is referred to the web version of this article.)

state $(i + 1)$, the latter being its broken parts. However, due to the distortion of the ROI during deformation (which was not considered in the cross-correlation) the inverse case can also happen, i.e. a son particle of state $(i + 1)$ can intersect several parent particles in state i (Fig. 8c). In such cases the parent-son relationship was attributed based on the maximum volume-overlap criterion. The tracking algorithm was applied to states 1 to 25 of the tensile test (at state 26 a large crack was already present in the sample, which hindered the evaluation of the later states). Fig. 8d illustrates the outcome of the analysis for states 7 and 8. The common intersection volume between IM particles of states 7 and 8 is colored in yellow, while particles regions without common intersection appear in light blue and red, respectively. The sum of the latter two is of about 10% and indicates the error of the correlation the analysis. However, the error of particle matching is much smaller; for example all particles of state 8 (sons) could be linked to pre-existing particles at state 7 (parents).

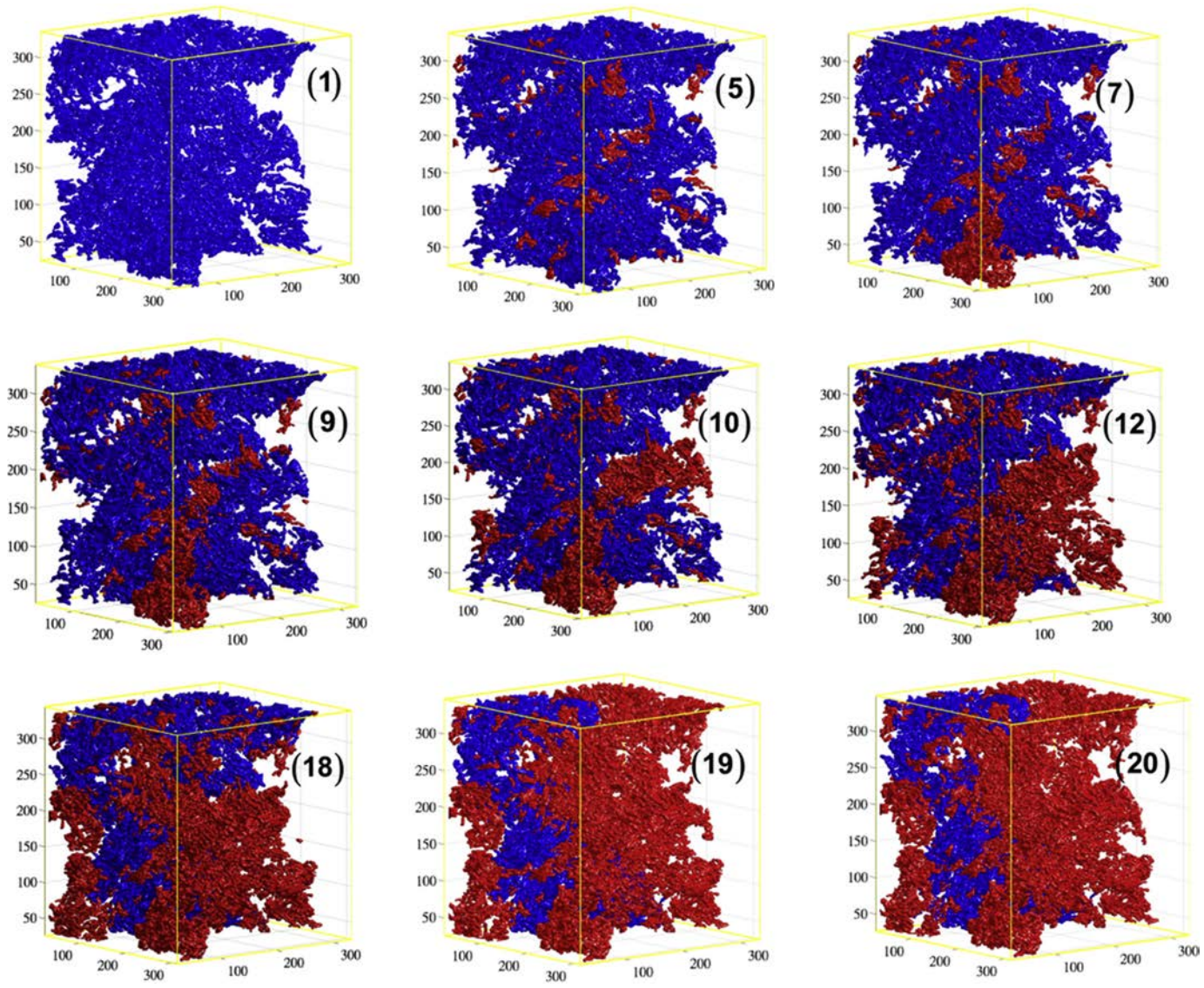

Fig. 9. Damage history of a complex IM structure from the undeformed state until specimen failure. The parents and sons are colored in blue and red, respectively. The units on the axis are given in voxels (1 voxel = 1.4^3 μm^3). (For interpretation of the references to color in this figure legend, the reader is referred to the web version of this article.)

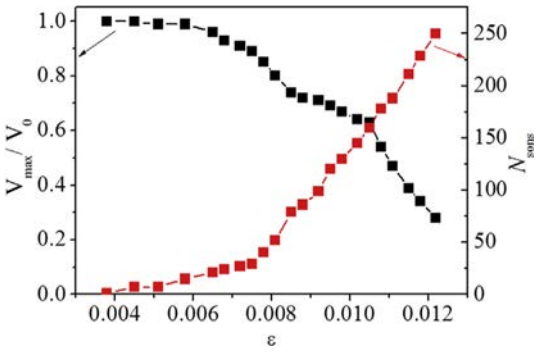

Fig. 10. Change in the number of sons and in the relative volume of the largest son of the IM structure found initially in the reconstructed ROI as a function of the applied strain. The numbers near the data points indicate the deformation states of the stress-strain curve (Fig. 6).

3.2. Break-up sequence of a large intermetallic particle

Fig. 9 shows the damage history of a large IM particle enclosed initially in a box of 300^3 voxels. Unbroken parts are colored in blue while the broken ones in red. The images are labeled according to the numbers marking the analyzed states in Fig. 6. The second image, corresponding to state no. 5 (close to the yield point, $\sigma_Y \cong 70$ MPa), emphasizes that particle rupture is active at this early stage of deformation, when small branches located far from the core of the complex particle already detach. This process continues until larger and larger parts break-off (states 7 to 18) leading to the complete loss of the load carrying capacity of the IM structure. Due to lack of visibility at the interior of the volume no significant change can be observed on the figures characterizing states 19 and 20, but as evidenced in Fig. 10 the "largest son" (as well as the smaller ones) continues to break-up. At state 20 the initial particle has numerous small and a few large sons. The latter are located at the core of the initial structure indicating the existence of a shielding mechanism that hinders plastic deformation in these regions.

Based on the tracking algorithm the number of broken parts and

the volume of the largest son were determined and are shown in Fig. 10 as a function of the applied strain. Both parameters indicate the existence of two different regimes, with different slopes. The transition from one regime to the other is better visible for the number of sons and takes place at state 11. The two curves give more insight into the damage sequence obtained visually from Fig. 9. According to them a smaller number of small clusters break-off already at the beginning of the tensile test reducing only slightly the volume of the largest son. Starting from state 11 the size as well as the detaching rate of the clusters becomes higher, which significantly reduces the volume of the largest son.

3.3. Geometrical analysis of the complex IM structure

In order to understand the break-up sequence of the IM network it is instructive to analyze its topological structure. It is known that rupture of rigid particles occurs at weak points [17,18], which are usually identified as long-thin branches. Coupling this information to the damage behavior described above one concludes that rupture of the complex IM phase must be related to its clustered configuration. In other words the IM 3D structure should be organized as an ensemble of denser regions (called clusters) connected by thin branches, which easily break upon loading. For testing this hypothesis a cluster identification algorithm consisting of three main stages has been developed (Fig. 11).

I) Determination of the skeleton of the particle by eroding it to a thickness of one voxel. This morphological operation done with ImageJ [8] (Fig. 11a).

II) Classification of the skeleton nodes (or singletons) as junction and end points (Fig. 11a).

III) In stage three each node of the skeleton (junction or end point) is considered as a separate cluster and the Euclidean distance between all pairs is calculated. The clusters are subsequently regrouped based on the minimum distance criterion, i.e. new clusters are formed by nearest-neighbors. This process is continued until all nodes belong to one cluster or an inconsistency criterion is matched.

The mathematical steps of stage III are the following:

1. At each step k, determine the distance $d^{(k)}(r,s)$ between all cluster-pairs r and s ($s \neq r$). Calculate their mean distance $\overline{d}^{(k)}$, and standard deviation $\sigma^{(k)}$.
2. Form the new clusters by grouping nearest-neighbors satisfying a certain consistency measure τ, which in the present case was defined as the ratio of the deviation of the nearest-neighbor distance $d_{n-n}^{(k)}(r,s)$ form the average $\overline{d}^{(k)}$, with regard to the standard deviation $\sigma^{(k)}$ (at each step k).

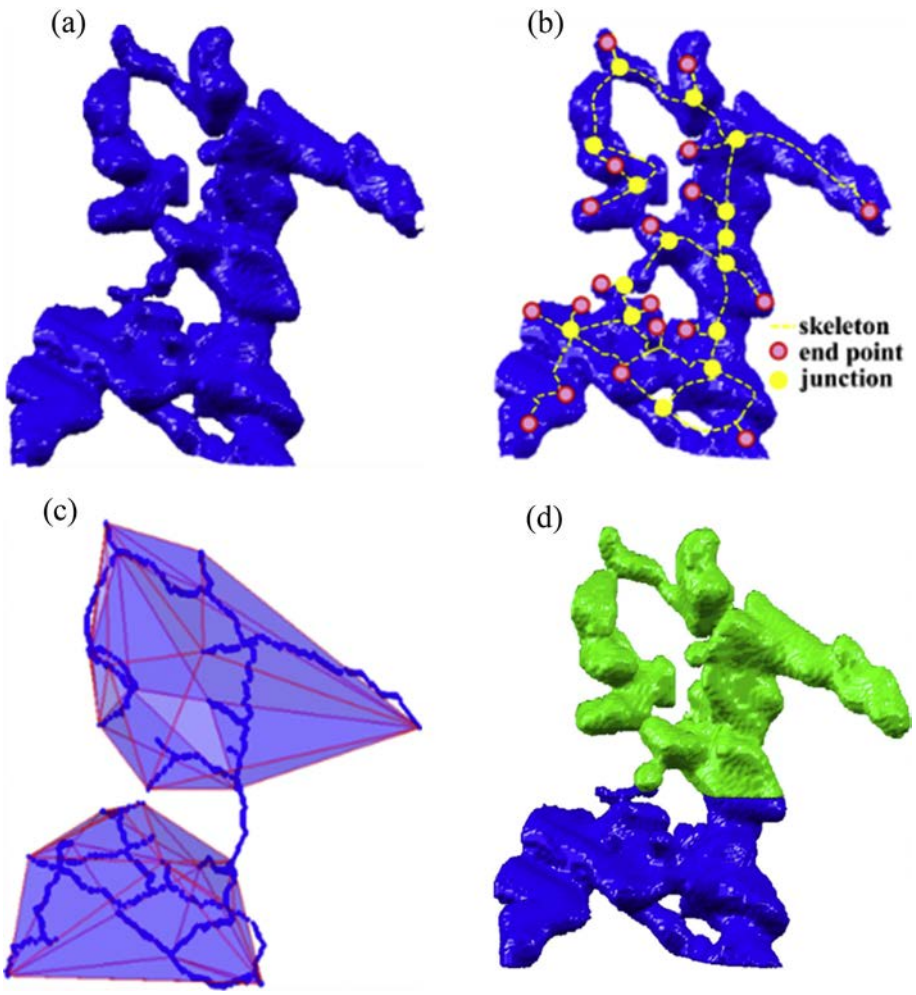

Fig. 11. Application of the cluster identifying algorithm to a simple particle. (a) Skeleton of the particle with the identified junction and end points. (b) Two identified clusters (blue and green) corresponding to a consistency criterion of $\tau \leq 2$. (c) Convex hulls of the clusters. (d) Parts determined by the present algorithm. (For interpretation of the references to color in this figure legend, the reader is referred to the web version of this article.)

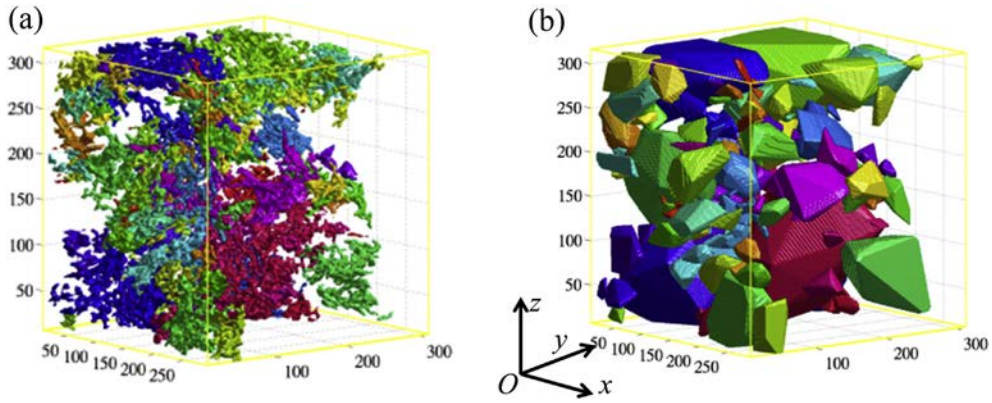

Fig. 12. (a) Clustered structure of the IM phase. (b) Convex hulls of the IM clusters.

$$\tau^{(k)}(r,s) \le \frac{\left|d_{n-n}^{(k)}(r,s) - \bar{d}^{(k)}\right|}{\sigma^{(k)}} \qquad (2)$$

3. Repeat steps 1 and 2 until all clusters satisfy the inconsistency criterion ($\tau^{(k)}(r,s) > \tau$) or they form one single cluster. In the present work the threshold vale of $\tau = 2$ was taken, which resulted in two clusters for the case of the selected particle (Fig. 11b). An alternative way for stopping the algorithm can be done by selecting a critical distance in the dendrogram [19].
4. Once the algorithm stopped a convex hull is constructed around each cluster [20] (Fig. 11c).

It is intriguing now looking for the connection between the clustered IM structure and the observed damage sequence as well as the mechanical behavior of the alloy. Recognizing that plastic deformation is negligible in regions with IM clusters one can approximate the structure of the complex alloy by that of a particle reinforced composite, where the particles correspond to the clusters identified in the IM structure. This is exemplified in Fig. 12(a) and (b) showing the clusters in the real structure and their convex hulls, respectively. The latter are the "effective particles" of the alloy and seem to have slightly different mechanical properties since their IM volume fraction changes with the size of the clusters. Fig. 13 summarizes the results obtained from the analysis of 15 different ROIs, each having a size of 300^3 voxels (420^3 μm^3). A power-law dependence between the IM volume fraction and cluster volume can be stated. Small clusters show a relatively large scatter, related to the higher variability of the structure at small scale, but in general they are denser than larger clusters. For clusters larger than $5{\cdot}10^5$ voxels, the volume fraction decreases towards the mean volume fraction of IM phases in the alloy, i.e. about 8−10% [6]. The observed inverse correlation between cluster size and IM density sheds light into their structure-property relationship. Since the "effective elastic properties" of the clusters should be a weighted average of its constituents it becomes evident that small clusters have a higher stiffness and therefore carry higher stress. Considering all weakest points (branches connecting the clusters) of equal strength one concludes that early break-off is more probable for small clusters than for larger ones.

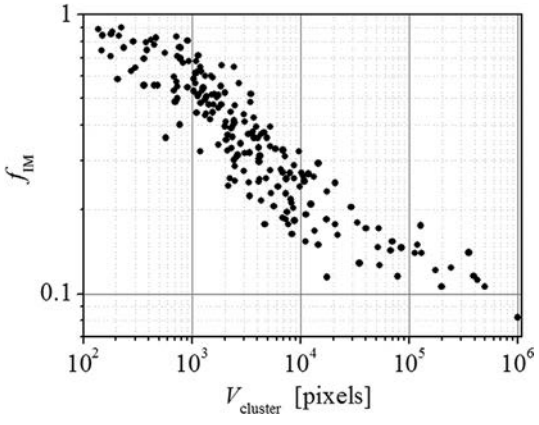

Fig. 13. Local IM volume fraction of clusters as a function of cluster volume.

3.4. Finite element modeling of the mechanical behavior

Besides its usefulness in understanding damage sequence of the IM structure the "effective particle" model can be used with FE calculations for obtaining local field parameters permitting to draw conclusions on strain localization. Based on SEM-DIC analysis (Fig. 3) showing that the Si phase hardly influences strain localization (at least at the early stage for deformation) the structure of the AlSi12Ni alloy can be considered in a first approximation similar to that of a particle reinforced composite consisting of a metallic matrix (mixture of Al and Si phases) and the IM clusters as particles. The two structures presented in Fig. 13a and b were meshed using Iso2mesh [21] and their plastic behavior was modeled with Zebulon [22]. The matrix was considered to have an elastoplastic behavior obeying the Voce law and its parameters were taken equal to that of an Al matrix reinforced with 12 wt% of Si particles. The IM structure and the "effective particles" were considered to deform only elastically. Fig. 14a and b shows the distribution of the equivalent plastic strain in the models with the complex real IM structure and the simplified particle reinforced composite, respectively. In both cases one can observe the presence of regions with local strains much larger or much smaller than the imposed overall value of 0.5%. This observation is similar to DIC results of SEM images (Fig. 4a), emphasizing the well-known fact that regions with IM clusters hardly deform, while strong strain localization develops in IM-free regions of the matrix. Although strain variability is higher in the real structure (Fig. 14a), the majority of the regions with high equivalent strain appear at identical positions in both images indicating that the simple model of the particle reinforced composite captures with good approximation strain localization taking place in the complex structure. This result is qualitative, but emphasizes well the double role played by IM clusters in damage which besides controlling the break-off

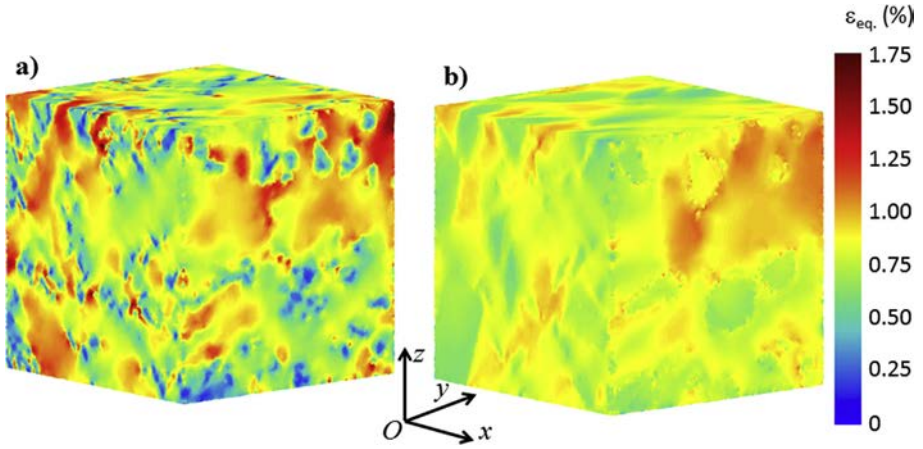

Fig. 14. Distribution of the equivalent plastic strain in the model with (a) complex IM 3D structure and (b) in the simplified "particle reinforced" composite. The distributions correspond to an overall tensile strain of 0.5% applied in the *Oz* direction.

sequence, determine shear band formation at the early stages of deformation, too. This localized plastic strain propagates later towards the core of the IM structure leading to decohesion of matrix-Si interfaces and crack formation.

4. Conclusions

Damage development during tensile straining of a cast AlSi12Ni alloy has been characterized in situ by SEM imaging and synchrotron X-ray micro-tomography. SEM images reveal the presence of two main damage mechanisms: a) break-up of the IM particles and b) decohesion of Al-Si interfaces. DIC analysis shows the presence of high strain localization in regions with low IM volume fraction.

The analysis of micro-tomography volumes recorded in situ during tensile deformation revealed that the clustered structure of the IM network plays a double role in damage. The convex hull associated to IM clusters contains a size dependent concentration of the IM phase. This concentration is higher in smaller clusters which carry therefore higher stress and have consequently higher probability to break-off earlier from the IM network than large clusters. IM clusters also control strain localization at the early stages of deformation, which later evolves into a more severe form of damage such as decohesion of Al-Si interfaces and formation of cracks.

Acknowledgement

The authors acknowledge the European Synchrotron Radiation Facility for beam time in the framework of proposal no. MA560 and Dr. E. Maire from INSA-Lyon for the provision of the miniaturized load frame.

References

[1] ASM Technical Report: Aluminum-silicon Casting Alloys: Atlas of Microfractographs, 2004.
[2] L.F. Mondolfo, Aluminium Alloys: Structure and Properties, Butterworths, London-Boston, 1976.
[3] J.R. Davis (Ed.), ASM Specialty Handbook: Aluminum and Aluminum Alloys, ASM International, 1993.
[4] S.Z. Lu, A. Hellawell, Modification of Al-Si alloys: microstructure, thermal analysis and mechanics, JOM 47 (1995) 38–40.
[5] Z. Asghar, G. Requena, H.P. Degischer, P. Cloetens, Three-dimensional study of Ni aluminides in an AlSi12 alloy by means of light optical and synchrotron microtomography, Acta Mater. 57 (2009) 4125–4132.
[6] Z. Asghar, G. Requena, F. Kubel, The role of Ni and Fe aluminides on the elevated temperature strength of an AlSi12 alloy, Mater. Sci. Eng. A527 (2010) 5691–5698.
[7] C.L. Chen, A. Richter, R.C. Thomson, Investigation of mechanical properties of intermetallic phases in multi-component Al–Si alloys using hot-stage nanoindentation, Intermetallics 18 (2010) 499–508.
[8] http://imagej.nih.gov/ij/.
[9] N.R. Pal, S.K. Pal, A review on image segmentation techniques, Pattern Recognit. 26 (1993) 1277–1294.
[10] A.M. Bruckstein, S.D. Yanowitz, A new method for image segmentation, Comput. Vis. Graph. Image Process 46 (1989) 82–95.
[11] http://www.fei.com/software/amira-3d-for-life-sciences/.
[12] M.A. Sutton, W. Wolters, W.H. Peters, W.F. Ranson, S.R. McNeill, Determination of displacements using an improved digital correlation method, Image Vis. Comput. 1 (1983) 133–139.
[13] G. Besnard, F. Hild, S. Roux, Finite-element displacement fields analysis from digital images: application to portevin-Le Châtelier bands, Exp. Mech. 46 (2006) 789–803.
[14] F. Hild, A. Münch, Y. Ousset, On the control of crack growth in elastic media, Comptes Rendus Mec. 336 (2008) 422–427.
[15] F. Hild, S. Roux, Comparison of local and global approaches to digital image correlation, Exp. Mech. 52 (2012) 1503–1519.
[16] J.Y. Buffiere, E. Maire, J. Adrien, J.P. Masse, E. Boller, In situ experiments with X-ray tomography: an attractive tool for experimental mechanics, Exp. Mech. 50 (2010) 289–305.
[17] N. Moulin, D. Jeulin, H. Klöcker, Stress concentrations in non-convex elastic particles embedded in a ductile matrix, Int. J. Eng. Sci. 47 (2009) 170–191.
[18] N. Moulin, E. Parra-Denis, D. Jeulin, C. Ducottet, A. Bigot, E. Boller, E. Maire, C. Barat, H. Klöcker, Constituent particle break-up during hot rolling of AA 5182, Adv. Eng. Mater. 12 (2009) 20–29.
[19] L. Kaufman, P.J. Rousseeuw, Finding Groups in Data: an Introduction to Cluster Analysis, John Wiley, New York, 1990, p. 119.
[20] G. Voronoi, J. für die Reine Angewandte Math. Crelle's J. 134 (1908) 198–287.
[21] http://iso2mesh.sourceforge.net/cgi-bin/index.cgi.
[22] http://www.zset-software.com/products/zebulon/.